ACS APPLIED MATERIALS & INTERFACES

Open Access
This article is licensed under CC-BY-NC-ND 4.0

www.acsami.org
Research Article

Metal Oxide–Metal Organic Framework Layers for Discrimination of Multiple Gases Employing Machine Learning Algorithms

Alishba T. John,[○] Jing Qian,[○] Qi Wang, Fabian S. Garay-Rairan, Y. M. Nuwan D. Y. Bandara, Artem Lensky, Krishnan Murugappan,* Hanna Suominen,* and Antonio Tricoli*

Cite This: *ACS Appl. Mater. Interfaces* 2025, 17, 27408–27421

Read Online

ACCESS | Metrics & More | Article Recommendations | Supporting Information

ABSTRACT: The increasing demand for gas molecule detection emphasizes the need for portable sensor devices possessing selectivity, a low limit of detection (LOD), and a large dynamic range. Despite substantial progress in developing nanostructured sensor materials with heightened sensitivity, achieving sufficient selectivity remains a challenge. Here, we introduce a strategy to enhance the performance of chemiresistive gas sensors by combining an advanced sensor design with machine learning (ML). Our sensor architecture consists of a tungsten oxide (WO_3) nanoparticle network, as the primary sensing layer, with an integrated zeolitic imidazolate framework (ZIF-8) membrane layer, used to induce a gas-specific delay to the diffusion of analytes, sharing conceptual similarities to gas chromatography. However, the miniaturized design and chemical activity of the ZIF-8 results in a nontrivial impact of the ZIF-8 membrane on the target analyte diffusivity and sensor response. An ML method was developed to evaluate the response dynamics with a panel of relevant analytes including acetone, ethanol, propane, and ethylbenzene. Our advanced sensor design and ML algorithm led to an excellent capability to determine the gas molecule type and its concentration, achieving accuracies of 97.22 and 86.11%, respectively, using a virtual array of 4 sensors. The proposed ML method can also reduce the necessary sensing time to only 5 s while maintaining an accuracy of 70.83%. When compared with other ML methods in the literature, our approach also gave superior performance in terms of sensitivity, specificity, precision, and *F*1-score. These findings show a promising approach to overcome a longstanding challenge of the highly miniaturized but poorly selective semiconductor sensor technology, with impact ranging from environmental monitoring to explosive detection and health care.

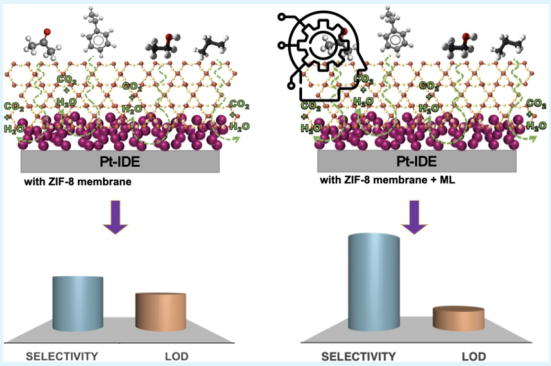

KEYWORDS: *chemiresistive, ZIF-8, nanoparticle networks, machine learning, gas discrimination, concentration prediction, evaluation studies, computer-assisted workflows*

1. INTRODUCTION

The field of gas sensors has witnessed significant advancements driven by the demand for effective monitoring and control of bio/chemical molecules across diverse applications, including environmental surveillance, industrial safety, and medical diagnostics.[1−4] Among various gas sensing technologies, chemiresistive sensors stand out for their simplicity in fabrication, ease of miniaturization, and integration into devices.[5,6] Their simple operational principle, based on the change in electrical resistance upon exposure to a target gas, provides advantages for signal processing and system integration. However, their poor selectivity hinders their widespread adoption in many applications.

The advancement in nanofabrication has led to several distinct approaches to enhance gas sensor performance. Surface modification strategies have emerged as a primary approach, with works ranging from chemical functionalization of metal and alloy nanoparticles[7] to targeted surface modifications of graphene oxide with SnO_2 nanoparticles and nitrogen doping for room-temperature NO_2 sensing.[8] This direction has extended to catalyst-enhanced surfaces, such as PdO-modified SnO_2 thin films for improved CO detection.[9]

Metal oxide-based approaches represent another significant direction, demonstrated through Pd-decorated ZnO nanoflowers for meat spoilage detection,[10] Si-doped WO_3 sensors for selective acetone detection in diabetes diagnosis,[11] and various hybrid functional nanomaterials.[12−14] These systems effectively utilize the intrinsic semiconducting properties of metal oxides, while enhancing their selectivity through precise material engineering. However, complex gas mixtures, varying real-world environmental conditions, the specificity of sensing

Received: January 30, 2025
Revised: March 17, 2025
Accepted: March 19, 2025
Published: April 23, 2025

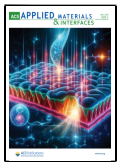

© 2025 The Authors. Published by American Chemical Society

materials, optimization difficulties, and potential interference effects contribute to the ongoing struggle in achieving high selectivity.[7]

A particularly promising direction has been the integration of metal−organic frameworks (MOFs). ZnO@ZIF-8 core−shell nanorods have demonstrated enhanced formaldehyde detection, utilizing the selective molecular sieving effect based on kinetic diameter.[7] Combinations of MOFs (ZIF-67 and MIL-88) with multiwalled carbon nanotubes have achieved impressive NO_2 detection with a low limit of detection (LOD) of 0.1 particles per million (ppm), benefiting from high surface area and the presence of Co/Fe elements.[7] More complex architectures such as α-Fe_2O_3−ZnO@ZIF-8 core−shell structures fabricated through atomic layer deposition and hydrothermal methods, have achieved high H_2S selectivity through a combination of high specific surface area, electron depletion layer effects, and the selective properties of the zeolitic imidazolate framework (ZIF-8) shell's surface functional groups and regular pores.[7]

Recognizing the intricate challenges of real-world gas sensing, such as environmental variability, temperature sensitivity, and cross-sensitivity, relying solely on material innovations may not provide a solution. Integrating electronic noses (e-noses)—capable of producing multidimensional patterns—and advanced machine learning (ML) methods to decipher complex, multivariate patterns introduced by e-noses,[1,8−10] has the potential to overcome current long-standing bottlenecks. Drawing inspiration from the discriminative prowess observed in the mammalian olfactory system, this integrated approach can be emulated in gas sensing technologies to enhance discrimination and measurement of target gases in diverse and complex environments.

E-noses generate multidimensional sensor response, encompassing both temporal and spatial dimensions. Temporal responses denote individual sensor reactions over time, while spatial responses indicate the collective sensor reactions of each E-nose component at a specific moment. Effectively managing complex multidimensional data demands thoughtful methods to extract meaningful patterns for distinguishing between target gases and measuring concentrations. Accurate classification of multivariate sensor signals poses an ongoing research challenge, emphasizing the crucial role of ML methods, including both traditional ML approaches and their modern deep learning (DL) counterparts. These methods have garnered attention for their effectiveness in overcoming challenges related to discriminating between gas molecules and identifying concentration in gas sensing applications.[10] Recent studies combining E-nose with ML methods, spanning from simple ML models like support vector machine (SVM)[11] to complex DL models like convolutional neural networks (CNN),[12] have demonstrated promising performance on various tasks. The ability of ML methods to discern patterns and make intelligent decisions based on complex data positions them as the key to unlocking the true potential of smart sensors for gas sensing applications.

Here, we present the development of an approach to discriminate the composition and concentration of a gas, relying on a custom-developed ML methodology to decipher the sensing response of an integrated ZIF-8 membrane-WO_3 nanoparticle network sensor array. The ZIF-8 membrane acts as a diffusion barrier, delaying or increasing the interaction of specific gas molecules with the WO_3 layer. The selective mechanism of our sensor array is achieved by leveraging the molecular sieve properties of the ZIF-8 membrane and its chemical affinity for specific gases. The ZIF-8 layer selectively decreases or facilitates diffusion of gas molecules based on their kinetic diameters and chemical interactions, which enhances the differentiation capability of the sensor array.

An ML methodology was developed to discern the unique sensor response patterns for each target gas, enabling effective discrimination of the gas type and concentration. To validate the performance gains resulting from the sensor fabrication method, we utilized eXplainable Artificial Intelligence (XAI) techniques, including ablation studies and permutation tests, were utilized. These methods provide deeper insights into the ML model's performance and further affirm that the improvement in pristine WO_3 sensor performance is attributed to the incorporation of the ZIF-8 membrane layer. This approach, combining advanced nanoscale architecture with ML methods, facilitates the effective processing and interpretation of dynamic sensor data, resulting in enhanced selectivity and overall performance with applications, including environmental monitoring, industrial safety, and medical diagnostics.

This study builds upon our previous work, where we explored the integration of metal oxide/ZIF-based materials for gas sensing. In this follow-up study, we significantly expand the scope by introducing a novel machine learning (ML) method to address key challenges in gas discrimination and concentration prediction. Also, we further stretched our proposed methodology to sense the gas mixtures. By leveraging the unique temporal and spatial sensing patterns of our material, our ML approach achieves unprecedented performance in accuracy, sensitivity, and specificity while enabling faster sensing times and lower limits of detection (LOD). It also maintained its performance in complex environments.

2. EXPERIMENTAL SECTION

2.1. Sensor Fabrication. Flame spray pyrolysis (FSP) system was employed to synthesize and directly deposit WO_3 fractal films onto platinum interdigitated electrodes (Pt-IDEs) (Figure S1). The fabrication process of WO_3 sensor films involved preparing a precursor solution with a tungsten atom concentration of 0.1 mol L^{-1}. This solution was prepared by dissolving ammonium (meta) tungstate hydrate (Sigma-Aldrich, purity >97%) in a mixture of diethylene glycol monobutyl ether (Sigma-Aldrich, purity >98.5%) and ethanol (Sigma-Aldrich, purity >99.5%) in a 1:1 v/v ratio. The precursor solution was delivered through a syringe pump at a constant rate of 5 mL min^{-1} and transformed into a fine spray with the assistance of 7 L min^{-1} oxygen at a consistent pressure drop of 2 bar. The spray was then ignited using a supporting premixed methane/oxygen flame (CH_4 = 1.8 L min^{-1}, and O_2 = 2 L min^{-1}). To maintain the substrate temperature below 150 °C, a water-cooled substrate holder was placed 20 cm above the burner. The sensor substrates were made of glass, and platinum interdigitated lines with 5 μm width and spacing were screen-printed on them, resulting in a total electrode area of 10 × 6 × 0.75 mm^3 (Microx Technologies, Spain). To ensure thermal stabilization and to prevent further nanoparticle sintering during sensing, the WO_3/Pt-IDE sensors were annealed at 500 °C for 5 h. Subsequently, ZnO was deposited on the annealed WO_3/Pt-IDE sensors using the same FSP technique. The precursor solution for ZnO deposition consisted of zinc naphthenate dissolved in xylene. For the conversion of ZnO to ZIF-8, a glass vial containing 310 mg of solid crystals of 2-methylimidazole (2-MIM) (Sigma-Aldrich) was placed inside a Teflon-lined stainless-steel autoclave, and the sensor substrates were positioned on a sample holder within the same autoclave. The autoclave was sealed and then heated at temperatures of 90 and 120 °C, with a gradual increase of 10 °C min^{-1}, in a gravity convection oven for a total of 18 h.[13]

https://doi.org/10.1021/acsami.5c02081
ACS Appl. Mater. Interfaces 2025, 17, 27408−27421

2.2. Material Characterization. Cross-sectional scanning electron microscopy (SEM) images were acquired using a Zeiss Ultraplus (FESEM) at an acceleration voltage of 2 kV. The morphology and microstructure of the materials were characterized by a Spectra 300 transmission electron microscope (TEM) at 300 kV. X-ray diffraction (XRD) patterns were obtained using a Bruker D2 Phaser XRD instrument, which was operated at 40 kV and 40 mA. The XRD scans covered a 2θ range of 5−80° with a scanning speed of 11 s^{-1} and a step size of 0.014°, using Cu Kα radiation. Fourier transform infrared (FTIR) spectrum was recorded using a Bruker α II FTIR spectrometer equipped with the PLATINUM ATR module. The FTIR analysis covered a spectral range of 4000−400 cm^{-1}. The X-ray photoelectron spectra (XPS) were obtained by Thermo Fisher K-Alpha+ XPS with monochromatic Al Kα X-ray tube (1486.6 eV). Electron paramagnetic resonance (EPR) spectra were collected by a Bruker EMXnano EPR spectrometer. The *g*-factor was calculated as

$$g = \frac{h\nu}{\mu_B B} \tag{1}$$

where h is the Plank's constant, ν is the microwave frequency used in the measurement (9.5 GHz), μ_B is the Bohr magneton, and B is the magnetic field strength at resonance.

2.3. Chemiresistive Gas Sensing Measurements. The 4-sensor virtual array consisted of two groups of sensors tested separately. Group 1 included WO_3 and ZnO/WO_3 sensors, while Group 2 consisted of (90 °C) ZIF-8/WO_3 and (120 °C) ZIF-8/WO_3 sensors. During gas sensing measurements, both sensors within each group were exposed to the same gas stream simultaneously under identical flow conditions (0.5 L min^{-1}) and at an operating temperature of 150 °C. The response data from both groups were analyzed collectively to evaluate the performance of the complete sensor array. Ethanol (10 ppm in N_2 (Coregas)), acetone (10 ppm in N_2 (Coregas)), ethylbenzene (10 ppm in N_2 (Coregas)), and propane (10 ppm in N_2 (Coregas)) were diluted in simulated air, prepared by mixing O_2 (BOC Ltd.) at a flow rate of 0.1 L min^{-1} and N_2 at a flow rate of 0.4 L min^{-1}. Precise control over the gas concentrations within the desired range of 0.1−1 ppm was achieved using a mass flow controller (Bronkhorst) while maintaining a constant total gas flow rate of 0.5 L min^{-1}. The gas sensing chamber, equipped with a Linkam hot plate, was set to a constant temperature of 150 °C using a temperature controller. Prior to gas sensing measurements, the sensors were stabilized in a controlled environment of 80% N_2 and 20% O_2 at a total flow rate of 0.5 L min^{-1} for 5 h at 150 °C to ensure a steady baseline resistance. During gas exposure, the oxygen concentration was maintained constant by keeping the O_2 flow rate unchanged, while the N_2 flow rate was adjusted to mix with the target gas, achieving the desired gas concentrations. This approach ensured consistent oxygen levels throughout all measurements, minimizing the impact of oxygen variations on the sensor response. The total flow rate of 0.5 L min^{-1} was maintained throughout to avoid any abrupt changes in the gas dynamics sensing test, and the total gas flow rate was set to 1 L min^{-1}, with the combination of acetone and propane selected. The acetone concentration was adjusted within the range of 0.05−0.5 ppm, while maintaining the propane concentration at 2 ppm. The flow of simulated air/target gases and temperature were controlled by using a custom Labview program. A digital multimeter (Keithley 2700) was used to measure the resistance of the sensors. The sensor response was calculated as

$$\frac{R_{air}}{R_{gas}} - 1 \tag{2}$$

where R_{air} and R_{gas} are the resistances of the sensor under simulated air and target gas conditions, respectively.

2.4. Machine Learning Methods. A total of 96 dynamic response curves were generated from four fabricated gas sensors—WO_3 nanoparticle network, ZnO/WO_3, (90 °C) ZIF-8/WO_3, and (120 °C) ZIF-8/WO_3—across all sensing measurements. These measurements involved four target volatile organic compounds (VOCs): acetone, ethanol, propane, and ethylbenzene, within a concentration range of 0.1−1 ppm, at a constant operating temperature of 150 °C. Each experiment was conducted three times to ensure the ML model's validation and performance reproducibility. The sensing chamber, equipped with automatic mass flow controllers, maintained a constant target gas concentration following a predefined protocol. Both the inflow of target VOC and simulated air were set at 1800 s for all six concentrations. The obtained dynamic sensor responses were baseline corrected and segmented into individual response−recovery curves, resulting in a total of 2700 samples in each curve. The sensor array's response−recovery curve followed a specific pattern, structured as 2700 × 4. During the model training process, each input was derived from a sample of the sensor array's response. Consequently, each input comprised a 1 × 4 vector representing the responses from four sensors at a particular concentration of a target gas species at a specific time.

In the controlled and stable experimental setting, we aggregated and treated sensor responses as if they were obtained from a sensor array. Instead of extracting features from the entire response−recovery curve, the ML model was directly trained on each sample collected by the four sensors, eliminating the need for an extensive feature extraction step. This approach facilitated on-the-go predictions based on spatial characteristics rather than temporal ones. Given that the sensor array responds to environmental changes simultaneously, the spatial characteristics are anticipated to be consistent. This consistency aids the model's predictions when sensors react to a specific target gas. The specially designed sensor array contributes to the distinctiveness of the response pattern to a particular target gas.

To enhance the overall capabilities of our developed sensors and ensure real-world applicability, we designed a two-stage multiclass classification model workflow capable of gas discrimination and concentration prediction. Utilizing the supervised ML algorithm eXtreme Gradient Boosting (XGB) model, the workflow involves a gas discrimination model predicting the gas species first, followed by individual concentration prediction models for each gas. This model workflow comprises one gas discrimination model and one concentration prediction model for each of the four target gases. The sensor array's response is initially fed into the gas discrimination model to identify the gas species, followed by input to the corresponding gas concentration model for quantifying the gas concentration. The final prediction for both gas discrimination and concentration is derived through a majority rule applied to the model predictions of each individual response sample from the sensor array's response−recovery curve. This approach allows for dynamic adjustment of the sensing time, eliminating the need to wait for the entire response−recovery curve to be collected while capturing the temporal information. For instance, the model can make predictions based on the first five response samples to discriminate and measure the gas concentration.

However, the experiment's concentration range is constrained to discrete concentrations between 0.1 and 1 ppm. Consequently, the training label for the concentration prediction model includes only six different concentrations. Since a regression model is optimized to minimize the error between the predicted and actual values, the model, when confronted with a limited and defined concentration range with an equal number of samples, may tend to predict the mean of the concentrations to achieve the lowest error. Therefore, training a regression model to predict the concentration range might not yield meaningful results. To address this, we reformulated the concentration prediction as a multiclass classification problem. In this approach, our model aims to categorize the sensor array's responses into relevant concentration categories.

To further ensure the quality of our ML workflow, we subjected the ML model's performance to three rounds of cross-validation using the leave-one-out method, aligning with the repetition of our sensing experiment three times. From the cross-validated results, we computed confusion matrices and classification metrics. The performance metrics were presented with their maximum and minimum ranges to statistically analyze the mode performance. Additionally, ablation[14] and permutation[15] studies were implemented to conduct a thorough evaluation and gain better explainability from the XGB

https://doi.org/10.1021/acsami.5c02081
ACS Appl. Mater. Interfaces 2025, 17, 27408−27421

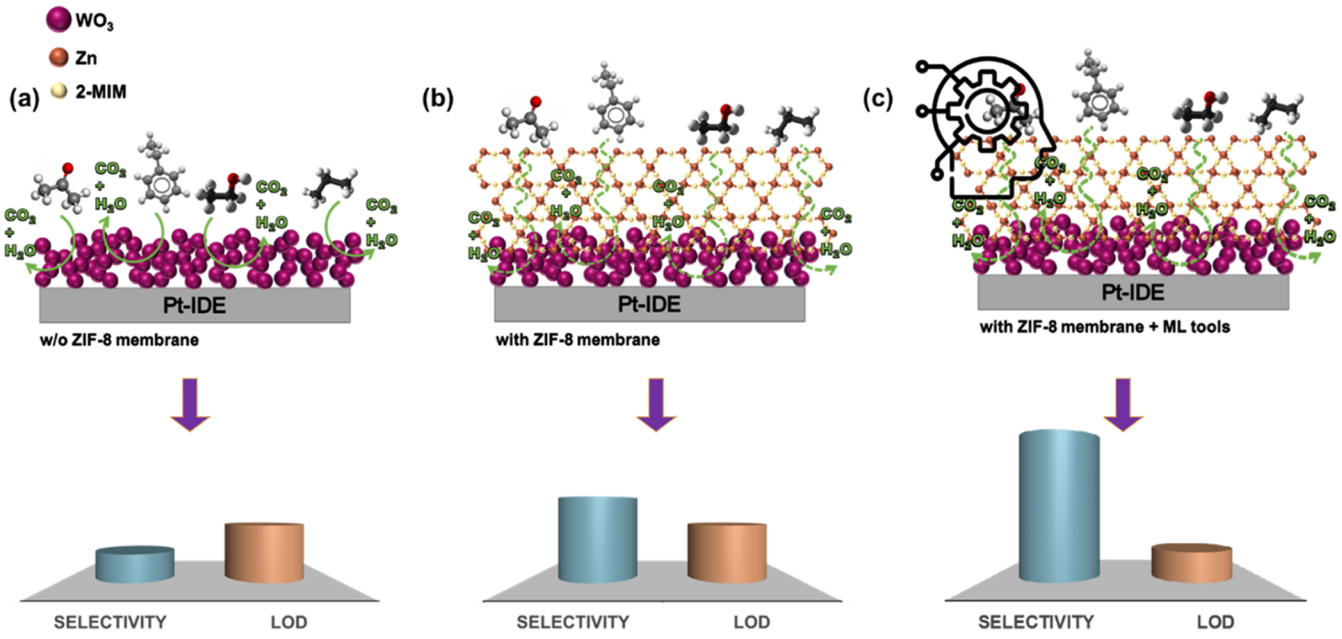

Figure 1. Schematic representation of our gas sensing mechanism. (a) WO_3 nanoparticle network, fabricated through direct aerosol deposition of flame-made nanoparticles, operates solely through electrocatalytic reactions with target gas molecules, resulting in a low level of selectivity and a high limit of detection (LOD). (b) ZIF-8/WO_3sensor created by depositing ZnO onto the WO_3 layer using FSP, followed by chemical vapor conversion to form ZIF-8. The inclusion of the ZIF-8 membrane enables selective diffusion of target gases, leading to some improvement in selectivity while still maintaining a relatively high LOD. (c) Integration of ML improves selectivity and decreases the LOD, hence enhancing the capabilities of gas sensor system.

models. This process ultimately aided in understanding each sensor's contribution to the sensing.

2.5. Proposed Workflow. The proposed workflow integrates ML to enhance sensor performance and assess the ML model's effectiveness, providing validation for the chosen sensing materials and fabrication process. Initially, the sensing material and fabrication process were designed to create prototype sensors. Subsequently, sensing experiments were conducted three times to collect experimental data for ML training and testing.

A two-stage ML modeling workflow was devised to make the ML pipeline applicable for real-time and real-world scenarios. First, the gas discrimination model was trained on target gases and concentrations from two out of three experiments, ensuring accurate discrimination of each target gas. Following this, the concentration prediction model was trained on each target gas and all concentrations, resulting in four concentration prediction models. After model training, response samples from four sensors underwent the gas discrimination model to assign gas species. A majority vote (MV) on the model predictions determined the final gas species and the applicable concentration prediction model. Incorrectly assigned gas species prompted the use of the corresponding concentration prediction model, underscoring the need for a highly accurate gas discriminator. The workflow evaluation occurred after the two-stage model predictions, where model inputs received two predictions for gas species and gas concentrations. Classification metrics and confusion matrices were computed for each experiment, serving as the testing set, and aggregated by calculating the mean.

To further validate the ML model, performance evaluation and statistical analysis were conducted using the same methods and measures as described above. A permutation test was employed to show that the model performance is statistically significant. Ablation studies were conducted to confirm the performance improvement achieved by adding additional sensors, informed by their sensing performance based on the sensing material and fabrication, contributing to the design and evaluation of the sensors.

3. RESULTS AND DISCUSSION

3.1. Sensing Mechanism Hypothesis and ML Incorporation. Figure 1 depicts our gas sensing concept relying on the redox reaction between the WO_3 nanoparticle network and target gas molecules (Figure 1a). Despite its effectiveness, this approach faces challenges related to low selectivity—a common issue in chemiresistive gas sensing applications—limiting the ability to distinguish between different gas species. To mitigate this limitation, we introduced a ZIF-8 membrane into our gas sensing system, as illustrated in Figure 1b. This involved depositing ZnO onto the WO_3 layer through nanoparticle aerosol deposition and then converting it via chemical vapor conversion to create the ZIF-8 membrane.[13] This addition enhances selectivity through factors such as chemical affinity and selective diffusion of target gases. To further enhance responsivity, we integrated ML methods into our system (Figure 1c). The integration of ML can significantly improve selectivity and substantially reduce the LOD capabilities of our sensors, this approach opening exciting possibilities for advancing the capabilities of gas sensing systems.

3.2. Sensor Characterizations. Figure 2 presents the morphological and structural characterizations of our developed sensors. Figure 2a represents a homogeneous film of WO_3 nanoparticle network with a thickness of 5.02 μm and a porosity of 98%. Figure 2b represents a homogeneous film of ZnO/WO_3 while Figure 2c,d represents ZIF-8/WO_3 converted at 90 and 120 °C, respectively. We observe from the SEM micrographs that upon increasing the conversion temperature of ZIF-8, the extrinsic porosity of ZIF-8 decreases and makes the overall structure dense. Figure S2a,b presents the TEM images of WO_3 nanoparticles collected from the flame-deposited films. The micrographs illustrate highly crystalline and porous spheroidal particles characterized by a similar size

https://doi.org/10.1021/acsami.5c02081
ACS Appl. Mater. Interfaces 2025, 17, 27408−27421

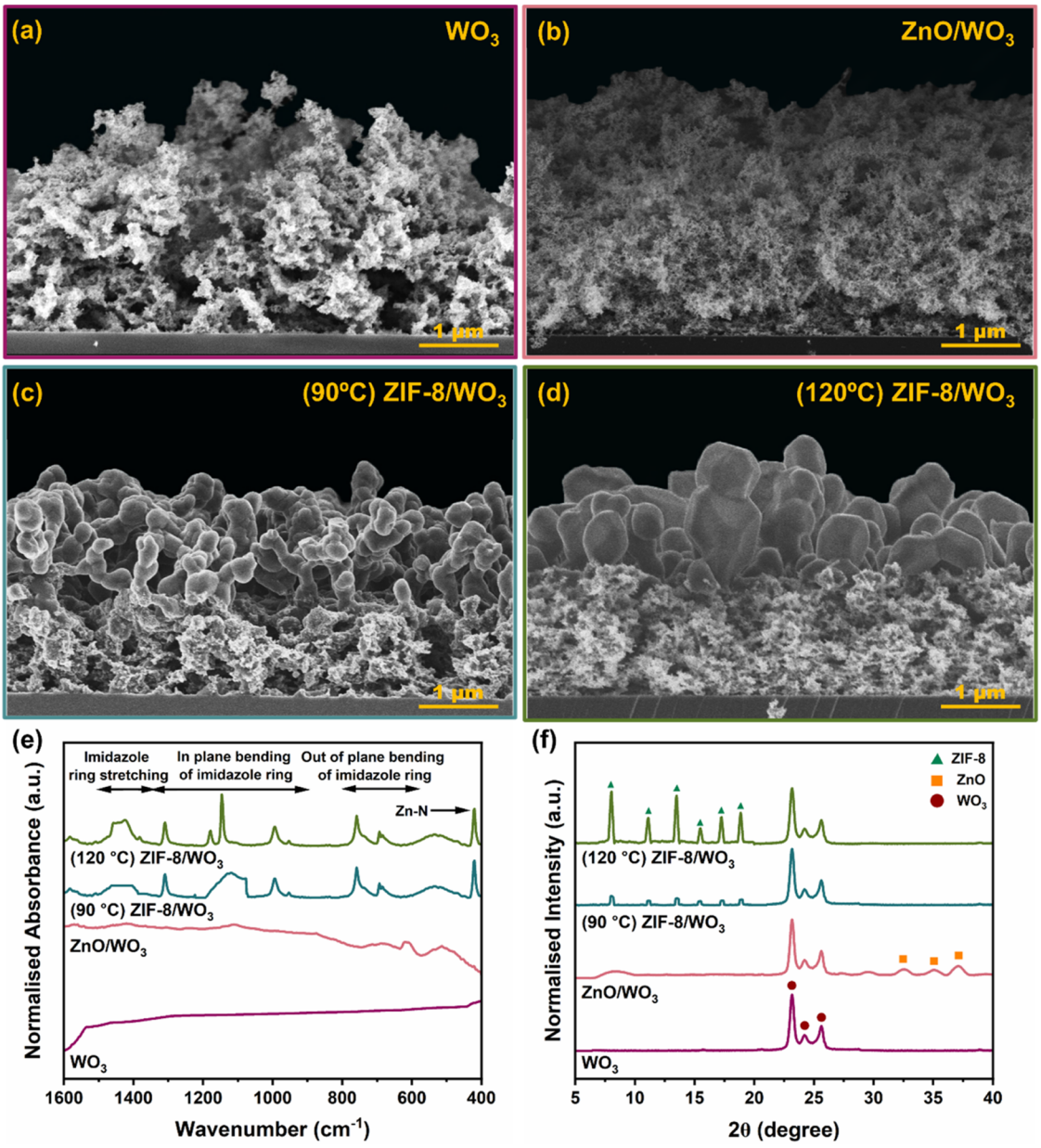

Figure 2. Morphology and structural characterization of fabricated sensor components. Cross-sectional images of (a) WO_3 nanoparticle network, (b) ZnO/WO_3, (c) (90 °C) ZIF-8/WO_3, and (d) (120 °C) ZIF-8/WO_3. (e) X-ray diffraction (XRD) pattern and (f) Fourier transform infrared (FTIR) spectrum of WO_3 (purple), ZnO/WO_3 (pink), (90 °C) ZIF-8/WO_3 (green), and (120 °C) ZIF-8/WO_3 (olive).

distribution as previously reported for flame synthesis of WO_3.[16−19] Figure S2c,d shows the TEM images of the ZnO/WO_3 nanoparticles, which also exhibit a similar size distribution and morphology as reported in previous flame-based fabrication studies.[20] Figure S2e−h displays the TEM images of 90 and 120 °C ZIF-8/WO_3, showing a well-defined, uniform morphology with high crystallinity. To confirm the structural conversion of ZnO to ZIF-8, FTIR and XRD were performed, as represented in Figure 2e,f, respectively. FTIR spectral analysis (Figure 2e) of ZnO shows the characteristic stretching bonds of Zn and Zn−O at 440 cm^{-1}. The replacement of Zn−O stretching with Zn−N stretching at 423 cm^{-1} and appearance of characteristic imidazole ring stretching (1500−1350 cm^{-1}), in-plane bending of imidazole ring (1350−900 cm^{-1}), and out-of-plane bending of imidazole ring (800−660 cm^{-1}) further confirm the reaction between ZnO and 2-MIM and resultant formation of ZIF-8.[13] From the XRD pattern (Figure 2f) of WO_3 nanoparticle network (circles) the characteristic peaks obtained at 2θ = 23.3, 23.6, and 24.2° correspond to the (002), (020), and (200) facets.[21] While the diffraction peaks obtained at 32, 34.6, and 36.4° correspond to (100), (002), and (101) planes of hexagonal ZnO wurtzite structure for ZnO/WO_3 (squares) films.[22] After the reaction of ZnO/WO_3 films with 2-methylimidazole (2-MIM), the appearance of diffraction peaks at 2θ = 7.3, 10.3, 12.7, 14.8, 16.4, and 18° corresponds to the (110), (200), (211), (220), (310), and (222) planes of crystalline sodalite ZIF-8 phase (triangles), thereby confirming complete conversion of ZnO.[13,23]

The XPS spectra of WO_3, ZnO/WO_3, (90 °C) ZIF-8/WO_3, and (120 °C) ZIF-8/WO_3 are represented in Figure S3. The W 4f spectrum (Figure S3a) displays peaks at ∼35.11 eV (W

https://doi.org/10.1021/acsami.5c02081
ACS Appl. Mater. Interfaces 2025, 17, 27408−27421

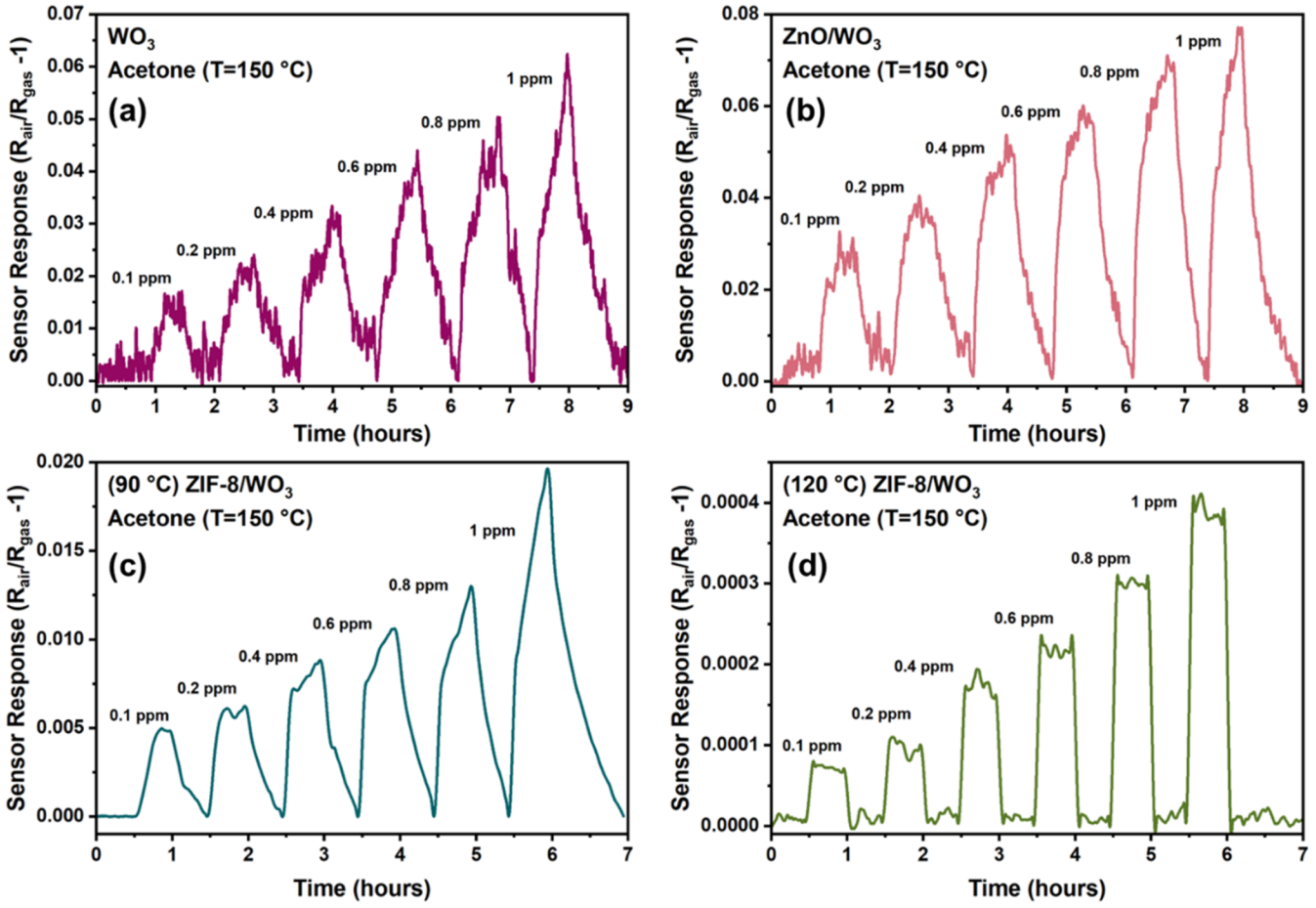

Figure 3. Dynamic sensing responses of (a) WO_3, (b) ZnO/WO_3, (c) (90 °C) ZIF-8/WO_3, and (d) (120 °C) ZIF-8/WO_3 toward acetone at 150 °C within the concentration range of 0.1−1 ppm.

$4f_{7/2}$) and ∼37.3 eV (W $4f_{5/2}$), confirming the presence of W^{6+} and indicating that the material is predominantly in its fully oxidized WO_3 state. The absence of lower-energy peaks suggests minimal reduction (e.g., to W^{4+} or W^{5+}) and good stoichiometry. The O 1s spectrum (Figure S3b) shows a primary peak at ∼529.99 eV, corresponding to lattice oxygen (W−O bonds) in WO_3, with a shoulder around ∼532 eV attributed to surface hydroxyl groups or adsorbed water. These features are typical for WO_3 materials under ambient conditions.[24] The W 4f spectrum (Figure S4a) exhibits peaks at ∼35.18 eV (W $4f_{7/2}$) and ∼37.27 eV (W $4f_{5/2}$), confirming W^{6+} as the dominant oxidation state, with no evidence of significant reduction to W^{4+} or W^{5+}. In the O 1s spectrum (Figure S4a), peaks at ∼528.2 and ∼531.6 eV correspond to lattice oxygen (O^{2-}) in the WO_3 framework and surface hydroxyl groups, respectively. The Zn 2p spectrum (Figure S4d) shows peaks at ∼1021.5 eV (Zn $2p_{3/2}$) and ∼1044.5 eV (Zn $2p_{1/2}$), confirming the presence of Zn^{2+} ions typical of ZnO, with Zn^{2+} fully incorporated into the oxide lattice.[25] These results indicate the successful integration of ZnO and WO_3, retaining their structural integrity. The O 1s spectrum (Figure S5b) reveals a primary peak at ∼530.2 eV, corresponding to lattice oxygen (O^{2-}) in WO_3, and a secondary peak at ∼532 eV, attributed to surface hydroxyl groups or adsorbed water. These features are consistent with the partial decomposition of ZIF-8, which promotes surface hydration. The W 4f spectrum (Figure S5a) shows peaks at ∼35.46 eV (W $4f_{7/2}$) and ∼37.62 eV (W $4f_{5/2}$), confirming W^{6+} as the primary oxidation state with no significant reduction. The Zn 2p spectrum displays peaks at ∼1021.61 eV (Zn $2p_{3/2}$) and ∼1044.1 eV (Zn $2p_{1/2}$), confirming the Zn^{2+} species. These results suggest partial decomposition of ZIF-8 into ZnO and the incorporation of Zn into the WO_3 matrix.[26] Similar results were observed for (120 °C) ZIF-8/WO_3 (Figures S6−S17).

3.3. Chemiresistive Gas Sensing Behavior and Response. The subsequent investigation aimed to evaluate the gas sensing capabilities of our hybrid membrane chemiresistor sensors. Figure 3 illustrates the sensor response of the WO_3 nanoparticle network film, ZnO/WO_3, (90 °C) ZIF-8/WO_3 and (120 °C) ZIF-8/WO_3 sensors toward varying concentrations of acetone, ranging between 0.1 and 1 ppm at 150 °C. The sensor array's responses to all four types of gases were plotted in Figures S6−S17. Under simulated air conditions, the WO_3 sensor interacts with the oxygen molecules, which capture free electrons from the WO_3 conduction band. This results in the formation of superoxide molecules (O_2^-) on the surface. At optimal operating temperatures, these superoxide molecules dissociate to form chemisorbed oxygen ions (O^-), which can additionally capture electrons to form oxide anions (O^{2-}). The EPR spectra of WO_3 and ZnO/WO_3 (Figure S4) exhibit prominent signals at g = 1.99 and 2.02, corresponding to O_2^- and O^-, respectively, which is in alignment with values reported in the literature.[27] These signals confirm the formation of active oxygen species on the surface of the sensing materials, which play a critical

https://doi.org/10.1021/acsami.5c02081
ACS Appl. Mater. Interfaces 2025, 17, 27408−27421

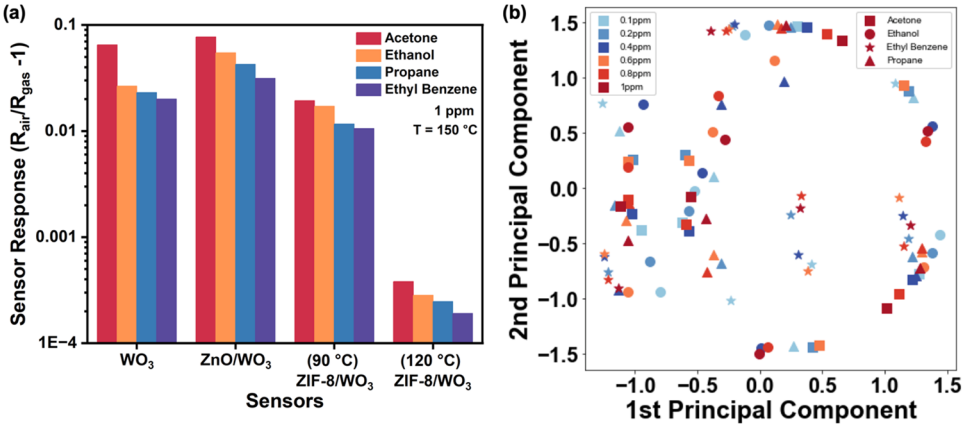

Figure 4. (a) Bar plot illustrating the responsivity of various sensors to 1 ppm of acetone, ethanol, propane, and ethylbenzene at 150 °C. (b) Principal component analysis (PCA) plot demonstrating responses of four tested gases within a concentration range of 0.1−1 ppm. Each data point in the figure represents a response curve of a specific target gas and concentration combination obtained by one of the four sensors. The shape represents the target gas species, and the color represents the concentration.

role in the gas sensing mechanism. This lowers the concentration of charge carriers and therefore increases the semiconductor resistance.[28−30] Upon exposure to a target gas (such as acetone), the gas molecules undergo a reaction with the iono-sorbed oxygen and release them from the WO_3 surface, resulting in the release of the previously trapped electrons back into the conduction band of WO_3, thereby decreasing the overall resistance. In the presence of a reducing gas, all of the sensors show a typical n-type sensing behavior, i.e., the resistance of the sensors decreases when a reducing gas is introduced into the sensing chamber and recovers back to its original resistance when the flow of target gas is stopped and stimulated air is introduced back into the system.

The responsivity study of all four fabricated sensors was carried out against other VOCs: ethanol, propane, and ethylbenzene each at a concentration of 1 ppm, as summarized in Figure 4a. The results clearly indicate that the ZnO/WO_3 sensor followed by the WO_3 nanoparticle network sensor is more reactive to almost all VOCs. By 90 °C conversion of the ZnO to a ZIF-8 membrane, the overall responsivity toward VOCs decreased by ∼30%. By further decreasing the overall porosity of the ZIF-8 membrane layer by increasing the conversion temperature to 120 °C, we observe a further decrease in overall responsivity by ∼90% for all tested gases. The considerable reduction in response for tested gases can be attributed to the diffusion barrier induced by the ZIF-8 membrane.[31]

Figure S5 represents the dynamic responses of the sensor array: WO_3, ZnO/WO_3, (90 °C) ZIF-8/WO_3, and (120 °C) ZIF-8/WO_3 in the presence of a gas mixture of propane (held at a constant concentration) and acetone (with varying concentrations). The ZIF-8-coated sensors, particularly (120 °C) ZIF-8/WO_3, exhibit well-defined and sharp response plateaus corresponding to different acetone concentrations, indicating superior selectivity and sensitivity. This performance is attributed to the molecular sieving effect of ZIF-8, which restricts propane diffusion while allowing acetone to interact with the sensing layer. In contrast, the WO_3 and WO_3/ZnO sensors show broader and less distinct response curves, suggesting reduced selectivity in the presence of propane. These results confirm the recognition ability of the sensor array, particularly the enhanced performance of the ZIF-8/WO_3 sensors in detecting and distinguishing acetone concentrations in a mixed gas environment.

3.4. ML Characterization Using Traditional Techniques. To visualize the responsivity to different gases of our developed four-sensor array, principal component analysis (PCA) was performed on the response−recovery curve of each of the four fabricated sensors across all four tested gases within the concentration range of 0.1−1 ppm, as illustrated in Figure 4b. For each target gas concentration combination, the response curves from four sensors were aggregated into a matrix to extract the first two principal components, allowing us to envision the response character distribution in a two-dimensional space. PCA is a common unsupervised learning method that is widely adopted in many fields.[32−34] Specifically in chemical sensing, if PCA could clearly group sensor responses into blobs, then there is no further need to use any supervised ML methods. Unfortunately, we did not observe any clearly recognizable groups in the visualized principal components. However, we noted three widely distributed and overlapping major clusters. These clusters show a tendency for gases of the same species but different concentrations to cluster together closely due to the similarity in the shape of the sensor response, with variations primarily arising from differences in response amplitude caused by different concentrations. The absence of clear clustering renders it impractical to differentiate between gas species or concentrations simply by PCA alone. This motivates the exploration of ML methods that could facilitate selective gas discrimination and accurate concentration prediction. We supplement the PCA results with additional graphical representations that better illustrate the model's classification performance. As observed in Figure S18, the matrix demonstrates a good aggregation and differentiation of the four gases in our machine learning models, reinforcing the quantitative results obtained from classification accuracy and other performance metrics.

3.5. Performance Evaluation of the Machine Learning Models. To address the limitations of PCA, we developed a two-stage ML model workflow. Our ML model workflow processes spatial features, represented by the sensor array's responses at a particular time slice, to make predictions. It employs a majority vote on multiple predictions to incorporate temporal information from the response curve. This approach

https://doi.org/10.1021/acsami.5c02081
ACS Appl. Mater. Interfaces 2025, 17, 27408−27421

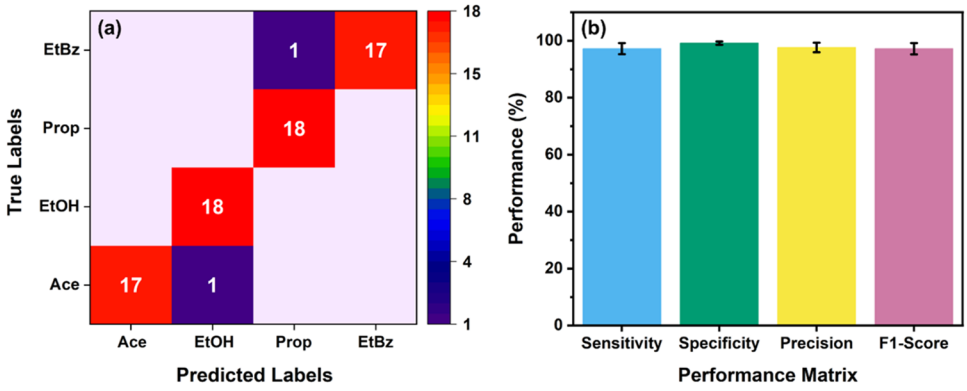

Figure 5. Performance evaluation of the gas discrimination model. (a) Confusion matrix analysis for gas discrimination model testing. (b) Bar plot representing performance metrics: sensitivity, specificity, precision, and *F*1-score.

enables the model to arrive at a final decision for both gas discrimination and concentration prediction. This workflow first distinguishes between gas species using the gas discrimination model and subsequently predicts their concentrations using the corresponding concentration prediction models based on the predicted target gas. In the initial step, we assessed the gas discrimination capability by generating a confusion matrix against all tested gases, as illustrated in Figure 5a. Analysis of the confusion matrix revealed an average accuracy of 97.22% to determine the gas species across the three-model cross-validations.

Supplementing the confusion matrix results, we computed the performance metrics—sensitivity, specificity, precision, and *F*1-score—depicted in the bar plot of Figure 5b. The performance metrics showcase the outstanding discrimination ability of our approach against various target gases, with sensitivity (97.22 ± 1.96%), specificity (99.17 ± 0.59%), precision (97.62 ± 1.68%), and *F*1-score (97.20 ± 1.98%). Also, a similar performance of the gas discrimination model is observed when we perturb the sensing responses. These findings demonstrate an accuracy of 97.22% with minimal standard deviation, emphasizing the robustness and reliability of our developed ML model to differentiate between target gases, thereby eliminating the selectivity issue.

To further extend the capabilities of the sensors and the proposed model, the sensors were tested under an acetone and propane gas mixture using a similar experiment protocol. Similar preprocessing was employed before the gas mixture response was introduced to the model. The gas mixture responses were added to the pure gas responses with different labels during the training process. We treated the gas mixture as the fifth class and maintained the multiclass classification setup, instead of the easier binary classification setup to test the model performance. The classification result on the separate test set showed 100% accuracy in distinguishing a gas mixture from pure gases. The model performance was cross-validated twice. All six gas mixture samples in each of the two test sets were correctly classified, resulting in a 100% accuracy in discriminating gas mixtures against pure gases (Figure S18).

To assess the gas discrimination model's robustness and provide insights into its functionality, we conducted ablation and permutation studies. In the ablation study, we trained the gas discrimination model with the omission of one sensor response at a time, measuring the classification accuracy to evaluate the impact of each sensor's contribution. As depicted in Table 1, the most significant performance drop occurred

Table 1. Ablation Study on Sensor Responses' Impact on Gas Discrimination Model's Performance

removed material	gas discrimination accuracy (%)	performance drop (%)
WO_3	94.44	2.78
ZnO/WO_3	95.83	1.39
90 °C ZIF-8/WO_3	87.50	9.72
120 °C ZIF-8/WO_3	84.72	23.5

when excluding the sensor response from the 120 °C ZIF-8 sensor, consistent with the instant saturation of this sensor compared with the others, as illustrated in Figure 3. Remarkably, removing sensors with the dense ZIF-8 structure resulted in a more pronounced performance decline, supporting the assertion that the microporous ZIF-8 structure enhances the sensor's selectivity.

Additionally, a permutation test was employed by randomly shuffling the target gas labels during the training process and evaluating the gas discrimination model's performance on the nonshuffled testing set. This permutation test, conducted with the leave-one-out method, involved 1000 iterations of cross-validation. Its aim was to test the null hypothesis that the relationship between the sensor response and the target gas could not be reliably learned by the XGB model used in the training step. The obtained *p*-value was less than 0.001, leading us to reject the null hypothesis, indicating that the gas discrimination model has indeed learned a reliable and statistically significant relationship between the sensor response and the target gas.

Following the evaluation of the gas discrimination model, the second step involved testing our two-step model for the concentration prediction abilities. Similar to the assessment of the gas discrimination model, we initially obtained a confusion matrix (Figure 6a) and performance matrices (Figure 6b) for all tested concentrations against all tested gases. The performance metrics indicated that our model achieved an average accuracy of 84.72% in predicting concentrations with sensitivity (86.11 ± 8.56%), specificity (97.22 ± 1.71%), precision (90.80 ± 4.28%), and *F*1-score (86.79 ± 7.81%).

3.6. Comparison of Predicted vs Actual Concentrations. To further confirm the effectiveness of our concentration prediction models, we meticulously compared the predicted concentrations against actual concentrations, as illustrated in Figure 7. The dashed diagonal line within the graph represents the perfect prediction scenario, while the plotted dots symbolize the predicted values. The minimal

https://doi.org/10.1021/acsami.5c02081
ACS Appl. Mater. Interfaces 2025, 17, 27408−27421

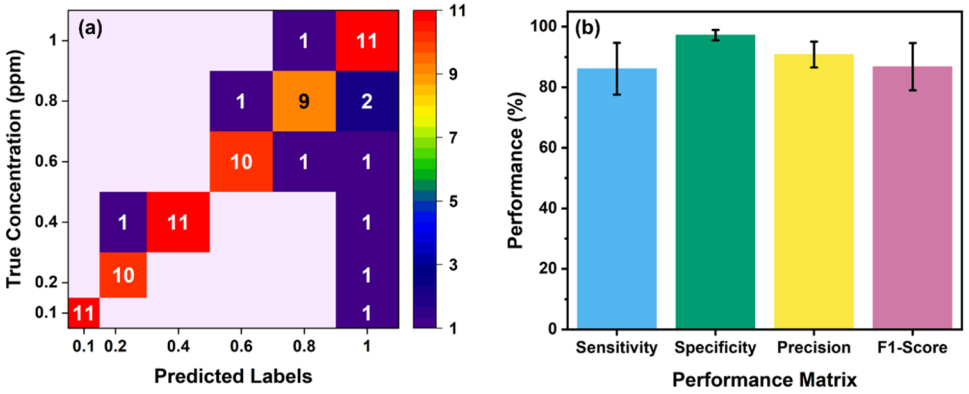

Figure 6. Performance evaluation of the concentration prediction model. (a) Confusion matrix analysis for concentration prediction model testing. (b) Bar plot representing performance metrics: sensitivity, specificity, precision, and *F*1-score.

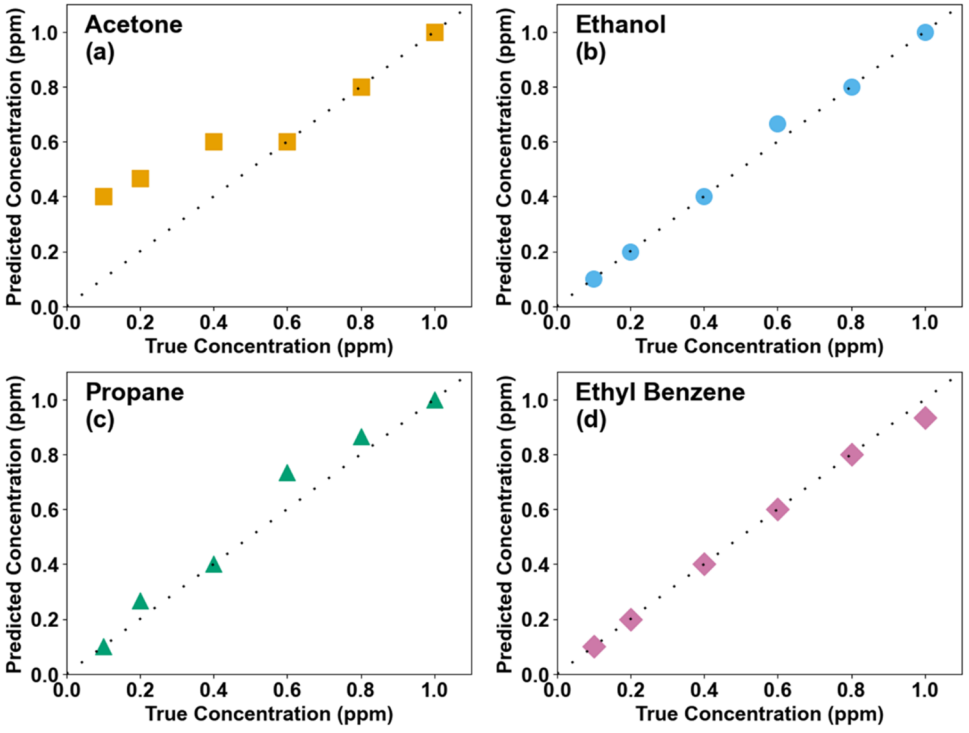

Figure 7. Quantitative concentration prediction for all of our tested target gases. The dotted line represents the perfect concentration prediction. (a) Acetone, (b) ethanol, (c) propane, and (d) ethylbenzene.

deviation observed from the actual concentrations attests to the accuracy of our prediction model. It is noteworthy that our concentration prediction model, despite relying on sensor responses, successfully demonstrated robust performance. This outcome highlights the pivotal role of our developed ML model in refining the sensor data and contributing to lower LOD. Specifically, the ML algorithms effectively discern subtle patterns in the sensor responses, enhancing the precision of concentration estimates, particularly for low concentrations. However, the relatively less favorable performance on acetone concentrations (Figure 7a) is attributed to the challenges posed by high noise levels in the first three concentrations and the similarity in amplitudes of the sensor responses within this range.

3.7. Response–Recovery Time Calculations Using Developed ML Model. Rapid response–recovery times in chemiresistive gas sensors are crucial parameters for swiftly detecting and identifying changes in the surrounding environment, facilitating the efficient real-time monitoring of toxic VOCs. These metrics are significantly influenced by the interaction between the VOCs and oxygen adsorption sites on the sensor surface. In our experimental investigation, the response and recovery times (calculated as 90% of the saturation) were calculated as 30 and 28 min, respectively. Recognizing the potential for further enhancement, we aimed to refine the analysis of the response time using our developed models. To accomplish this, we conducted a comprehensive examination of the shortest time required by our models, encompassing both gas discrimination and concentration prediction, to yield responses with the highest accuracy. The implementation of the majority rule empowers the ML model to make predictions within an arbitrary period provided we have more than three response samples. Figure 8 illustrates the

https://doi.org/10.1021/acsami.5c02081
ACS Appl. Mater. Interfaces 2025, 17, 27408–27421

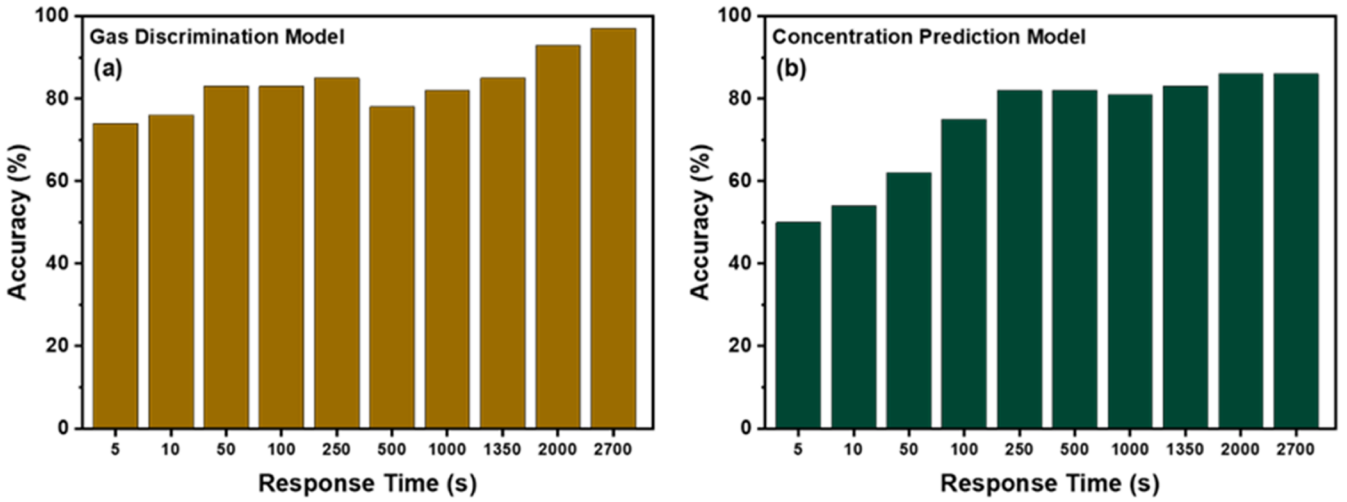

Figure 8. Accuracy trends of our developed (a) gas discrimination and (b) concentration prediction models at varying sensing times.

accuracy trends of our developed gas discrimination and concentration prediction models at varying sensing times.

We varied the sensing time from 5 s to the entire response and recovery time. As depicted in Figure 8a, for gas discrimination, the accuracy in prediction reached 70.83% with just 5 s of sensing time. The model's performance increased incrementally as the sensing time increased, reaching 97.22% accuracy with the entire response−recovery curve. The observed performance increases with longer sensing times, suggesting that the sensors formed a unique response pattern to characterize a specific gas. Since the model used a majority vote for the final prediction, the increased performance with longer sensing times indicated improved correct predictions. However, a drop was observed in Figure 8a when the sensing time reached 500 s, followed by an increase again. One possible explanation could be that the sensors' response to the chemical analyte started slowing down, and sensors fabricated with different materials responded to saturation at different rates, causing a deviation from the learned pattern and resulting in decreased performance. Also, as the model was predicting on each sample, there could be some noise on the sample and caused the wrong prediction.

For our concentration prediction model (Figure 8b), the model performed poorly with just 5 s; however, as the sensing time increased, the model's performance steadily rose from 50.00 to 84.72%. The model achieved 77.78% accuracy in just 250 s. Interestingly, the performance increased rapidly as the sensing time increased to 250 s but slowed with further increases, mirroring the sensor responses. Since the concentration prediction model followed the gas discrimination model, falsely predicted gas samples would be fed into the wrong concentration prediction model, resulting in incorrect predictions. Predicting concentrations requires specific patterns in sensor responses, namely, the response amplitude. Relying solely on patterns from gas discrimination tasks is not enough for accurate predictions at shorter sensing times. In conclusion, the ML has the potential to significantly reduce the sensing time required for gas discrimination and gas concentration prediction.

Following determination of the optimal response time (250 s for both models), we proceeded to calculate the LOD. Table 2 presents a comparative analysis between experimentally calculated LOD (utilizing the entire response curve of 3600 s) and ML-derived LOD (based on the first 250 s of data for response determination) for all developed sensors and tested VOCs. We observed that the responses acquired through the expedited ML process significantly reduced the LOD. This supported our initial hypothesis that leveraging our developed model can enhance the analysis of response−recovery times, thereby improving the assessment of the LOD for our developed sensors. The LOD was calculated based on 3 times the noise standard deviation from the sensor response curve within the time required for an accurate ML prediction,[35] i.e., 5 s.

Table 2. Comparison of Experimentally Observed and ML-Derived LOD (ppb)[a]

	WO_3		ZnO		90 °C ZIF-8		120 °C ZIF-8	
	exp	ML	exp	ML	exp	ML	exp	ML
acetone	196	12	441	22	37	6	27	0.19
ethanol	114	9	366	16	27	8	11	0.16
propane	509	5	240	8	77	3	90	0.14
ethylbenzene	185	5	106	7	169	4	64	0.08

[a]ppb: particles per billion; exp: experimental; ML: machine Learning.

3.8. Comparison of Model Accuracy with Those Reported in the Literature. We performed a comparative analysis of our models with those documented in the literature, which have demonstrated strong performance in chemical sensor responses through experimental validations, including convolutional neural network + long short-term memory (CNN + LSTM),[36] convolutional long short-term memory (CLSTM),[37] XGBoost,[38,39] and support vector machine (SVM),[40,41] as represented in Figure 9. We observed that our model showcased a high accuracy in discriminating between different gas species with 97.22% accuracy. Additionally, the model exhibited a commendable 84.72% accuracy in predicting concentrations. While the accuracy of our model closely aligned with that of the CNN + LSTM model in concentration prediction tasks, our model presents distinct advantages. Notably, it necessitates fewer input variables and imposes significantly lower computational demands. In contrast, the CNN + LSTM model entailed the utilization of millions of parameters, underscoring the computational efficiency of our XGB + MV model, which required only a minimal parameter set. This efficiency contributed to the

https://doi.org/10.1021/acsami.5c02081
ACS Appl. Mater. Interfaces 2025, 17, 27408−27421

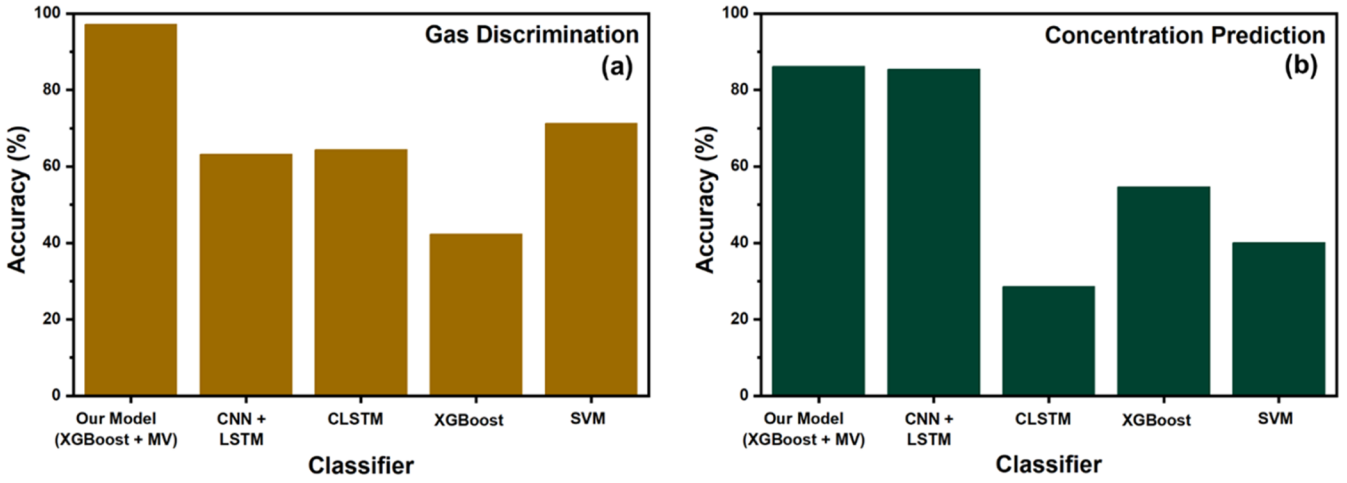

Figure 9. Comparison of ML models' performances on both tasks. (a) Model accuracy in discriminating between gas types. (b) Model accuracy in predicting concentrations.

Table 3. Comparative Analysis of Chemiresistive Gas Sensors Using ML[a]

sensor system	target gas	LOD (ppb)	response time	recovery time (s)	ML algorithm	accuracy (%)	ref
(120 °C) ZIF-8/WO_3	acetone	0.19	5 s	10	XGBoost + MV	97.22	this work
WO_3 nanoplates	formaldehyde	200	60 s	90	MLP	96.9	41
commercial sensors	VOC mixtures		20 min		LDA	79	42
SnO_2 hollow spheres	formaldehyde		190 s	35	RF	85.93	43

[a]MV = majority vote; MLP = multilayer perceptron, LDA = linear discriminant analysis, RF = random forest.

practicality and effectiveness of our proposed gas sensing system.

Comparison of our work with other VOC chemiresistive gas sensors is summarized in Table 3. ZIF-8-based chemiresistive gas sensors, as well as other metal oxide sensors, have been extensively explored for VOC detection due to their high selectivity and tunable surface properties. WO_3 nanoplates have been developed for formaldehyde detection, achieving a LOD of 0.2 ppm with a response time of 60 s and a recovery time of 90 s, while employing an SVM-based ML approach to enhance accuracy to 95%.[41] Similarly, commercial VOC mixture detection sensors utilizing LDA are limited by longer response times (~20 min) and lower accuracies (78%).[42] SnO_2 hollow spheres have also been employed for formaldehyde detection, demonstrating an LOD of 190 ppm and moderate response/recovery times of 35 s, coupled with an RF-based ML algorithm providing an accuracy of 85.93%.[43] Our study presents a (120 °C) ZIF-8/WO_3-based sensor that achieves an exceptionally low LOD (0.19 ppb) for acetone, with rapid response and recovery times (5 and 10 s, respectively) and high accuracy (97.22%) using an XGBoost + MV model. These results highlight the superior performance of our sensor compared to other state-of-the-art systems in the literature, particularly in terms of sensitivity, speed, and selectivity.

The selectivity mechanism of the ZIF-8-coated sensors relies on both material design and machine learning to achieve high levels of selectivity and sensitivity. The ZIF-8 membrane acts as a molecular sieve, selectively delaying or restricting the diffusion of gas molecules based on their size, shape, and chemical affinity. The selective diffusion rates enhance the relative sensor's response to specific target analytes, significantly enhancing selectivity, while reducing overall responsivity—by approximately 30% for the (90 °C) ZIF-8/WO_3 sensor and up to 90% for the (120 °C) ZIF-8/WO_3 sensor.

The advanced ML model compensates the reduced responsivity by analyzing subtle spatial and temporal patterns in the sensor array's response. This synergy is evident from the ablation study (Table 1), where the exclusion of the (120 °C) ZIF-8/WO_3 sensor resulted in a 23.5% drop in gas discrimination accuracy. The ML approach extracts meaningful insights from the sensor signals and ensures robust gas discrimination and concentration prediction, achieving accuracies of 97.22 and 84.72%, respectively. This combination of selective material properties and intelligent data processing highlights the system's ability to overcome traditional limitations of chemiresistive gas sensors, offering a powerful solution for applications in different practical applications.

The major limitation of this work was that the sensor array's signals were being aggregated virtually by strictly controlling the sensing chamber rather than being collected at the same time. Also, our work only attempted to discriminate gas species and gas concentrations rather than explore the potential of resolving the longstanding limitations of MOX sensors. Also, due to the limited concentration range, the concentration prediction task was converted to classification rather than regression. Future work will focus on using ML to address the limitations of MOX sensors, such as cross-sensitivity, lack of selectivity, and high LOD. We aim to expand the applicability of MOX sensors to wider application domains, such as health care, environmental, and national security.

4. CONCLUSIONS

Our work presents a comprehensive and innovative strategy to overcome challenges in chemiresistive gas sensing, addressing issues of low selectivity and slow response time while also improving the LOD. Through the incorporation of a ZIF-8 membrane into our nanoscale sensing architecture, we achieved improved selectivity, capitalizing on factors like

https://doi.org/10.1021/acsami.5c02081
ACS Appl. Mater. Interfaces 2025, 17, 27408−27421

selective diffusion of target gases. However, recognizing the persistent challenges of principal component approach approaches, in discerning between different gas species and accurately predicting concentrations with our four-sensor array, we introduced a two-step ML model. This integrated approach resulted in a robust and efficient gas sensing system. Our developed ML model demonstrated exceptional performance in discriminating between gas species and accurately predicting concentrations. The reliability of the model was emphasized by consistently high sensitivity (97.22 ± 1.96%), specificity (99.21 ± 0.59%), precision (97.62 ± 1.68%), and *F*1-score (97.20 ± 1.98%) metrics. Also, the ablation studies showed a significant contribution of the sensor with 120 °C ZIF-8 nanostructure to the gas discrimination performance, which further supported the experimental findings of the ZIF-8 nanostructure. The permutation test implied statistical significance of our model's performances in comparison with random guesses. Furthermore, our concentration prediction model exhibited precise estimates, even for low concentrations, contributing to a lower LOD and enhancing the overall utility of the gas sensing system. Comparative analysis with established models confirmed the higher accuracy of our model in discriminating gas species and its commendable accuracy in predicting concentrations. Therefore, our approach, combining a selective molecular diffusion barrier with an innovative ML model, offers a promising solution to some of the key longstanding challenges of chemiresistive gas sensing. This work represents an advancement in chemiresistive gas sensing by not only enhancing material performance but also leveraging machine learning for unprecedented levels of accuracy, speed, and explainability. The novel integration of ML highlights the potential for real-time applications and provides a pathway for further innovation at the interface between materials science and intelligent systems.

■ ASSOCIATED CONTENT

Supporting Information

The Supporting Information is available free of charge at https://pubs.acs.org/doi/10.1021/acsami.5c02081.

Photograph of the substrate, TEM image for the sensors, XPS spectra, EPR spectrum, sensor array's response to mixture gas, acetone, ethanol, ethylbenzene, and propane, scatter plot of machine learning outputs, and confusion matrices for gas discrimination with mixture gas and interfering gas (PDF)

■ AUTHOR INFORMATION

Corresponding Authors

Krishnan Murugappan − *Nanotechnology Research Laboratory, Research School of Chemistry, College of Science, The Australian National University, Canberra, ACT 2601, Australia; Commonwealth Scientific and Industrial Research Organization (CSIRO), Mineral Resources, Clayton South, VIC 3169, Australia;* orcid.org/0000-0002-6845-4653; Email: krishnan.murugappan@csiro.au

Hanna Suominen − *School of Computing, College of Engineering, Computing and Cybernetics and School of Medicine and Psychology, College of Health and Medicine, The Australian National University, Canberra, ACT 2601, Australia; Department of Computing, Faculty of Technology, University of Turku, 20014 Turku, Finland;* Email: hanna.suominen@anu.edu.au

Antonio Tricoli − *Nanotechnology Research Laboratory, Research School of Chemistry, College of Science, The Australian National University, Canberra, ACT 2601, Australia; Nanotechnology Research Laboratory, School of Biomedical Engineering, Faculty of Engineering, The University of Sydney, Camperdown, NSW 2006, Australia;* orcid.org/0000-0003-4964-2111; Email: antonio.tricoli@sydney.edu.au

Authors

Alishba T. John − *Nanotechnology Research Laboratory, Research School of Chemistry, College of Science, The Australian National University, Canberra, ACT 2601, Australia*

Jing Qian − *School of Computing, College of Engineering, Computing and Cybernetics, The Australian National University, Canberra, ACT 2601, Australia*

Qi Wang − *Nanotechnology Research Laboratory, School of Biomedical Engineering, Faculty of Engineering, The University of Sydney, Camperdown, NSW 2006, Australia*

Fabian S. Garay-Rairan − *Nanotechnology Research Laboratory, School of Biomedical Engineering, Faculty of Engineering, The University of Sydney, Camperdown, NSW 2006, Australia;* orcid.org/0000-0001-8863-5673

Y. M. Nuwan D. Y. Bandara − *Nanotechnology Research Laboratory, Research School of Chemistry, College of Science, The Australian National University, Canberra, ACT 2601, Australia*

Artem Lensky − *School of Engineering and Technology, The University of New South Wales, Canberra, ACT 2612, Australia; Nanotechnology Research Laboratory, School of Biomedical Engineering, Faculty of Engineering, The University of Sydney, Camperdown, NSW 2006, Australia*

Complete contact information is available at: https://pubs.acs.org/10.1021/acsami.5c02081

Author Contributions

○A.T.J. and J.Q. contributed equally to this work.

Notes

The authors declare no competing financial interest.

■ ACKNOWLEDGMENTS

K.M., A.L., H.S., and A.T. acknowledge financial support from the Department of Defence and Australian Research Council for the National Intelligence and Security Discovery Research Grants (NISDRG) Program (NS210100083). This research was funded by and has been delivered in partnership with Our Health in Our Hands (OHIOH), a strategic initiative of the Australian National University, which aims to transform health care by developing new personalized health technologies and solutions in collaboration with patients, clinicians, and health care providers. The authors acknowledge the facilities and the scientific and technical assistance of Microscopy Australia at the Centre for Advanced Microscopy, Australian National University, a facility that is funded by the University and the Federal Government. J.Q. is funded by the National Intelligence and Security Discovery Research (NISDR) Grant ID: NS210100083. A.T. gratefully acknowledges the support of the Australian Research Council for a Future Fellowship (FT200100939) and Discovery grant DP190101864. A.T. also acknowledges financial support

from the North Atlantic Treaty Organization Science for Peace and Security Programme project AMOXES (#G5634).

REFERENCES

(1) John, A. T.; Murugappan, K.; Nisbet, D. R.; Tricoli, A. An Outlook of Recent Advances in Chemiresistive Sensor-Based Electronic Nose Systems for Food Quality and Environmental Monitoring. *Sensors* **2021**, *21* (7), No. 2271.
(2) Yang, L.; Qin, M.; Zhang, G.; Yang, J.; Yang, J.; Zhao, J. Progress of sensitive materials in chemiresistive sensors for detecting chemical warfare agent simulants: A review. *Rev. Anal. Chem.* **2023**, *42* (1), No. 20220052.
(3) Majhi, S. M.; Mirzaei, A.; Kim, H. W.; Kim, S. S.; Kim, T. W. Recent advances in energy-saving chemiresistive gas sensors: A review. *Nano Energy* **2021**, *79*, No. 105369.
(4) Shetty, S. S.; Jayarama, A.; Karunasagar, I.; Pinto, R. A review on chemi-resistive human exhaled breath biosensors for early diagnosis of disease. *Mater. Today: Proc.* **2022**, *55*, 122−126.
(5) Bag, A.; Lee, N. E. Recent advancements in development of wearable gas sensors. *Adv. Mater. Technol.* **2021**, *6* (3), No. 2000883.
(6) Majhi, S. M.; Mirzaei, A.; Kim, H. W.; Kim, S. S.; Kim, T. W. Recent advances in energy-saving chemiresistive gas sensors: A review. *Nano Energy* **2021**, *79*, No. 105369.
(7) Tian, H.; Fan, H.; Li, M.; Ma, L. Zeolitic imidazolate framework coated ZnO nanorods as molecular sieving to improve selectivity of formaldehyde gas sensor. *ACS Sens.* **2016**, *1* (3), 243−250.
(8) Park, S. Y.; Kim, Y.; Kim, T.; Eom, T. H.; Kim, S. Y.; Jang, H. W. Chemoresistive materials for electronic nose: Progress, perspectives, and challenges. *InfoMat* **2019**, *1* (3), 289−316.
(9) Cheng, L.; Meng, Q.-H.; Lilienthal, A. J.; Qi, P.-F. Development of compact electronic noses: A review. *Meas. Sci. Technol.* **2021**, *32* (6), No. 062002.
(10) Yaqoob, U.; Younis, M. I. Chemical gas sensors: Recent developments, challenges, and the potential of machine learning—A review. *Sensors* **2021**, *21* (8), No. 2877.
(11) Tarttelin Hernández, P.; Hailes, S. M.; Parkin, I. P. Cocaine by-product detection with metal oxide semiconductor sensor arrays. *RSC Adv.* **2020**, *10* (47), 28464−28477.
(12) Liu, H.; Meng, G.; Deng, Z.; Nagashima, K.; Wang, S.; Dai, T.; Li, L.; Yanagida, T.; Fang, X. Discriminating BTX molecules by the nonselective metal oxide sensor-based smart sensing system. *ACS Sens.* **2021**, *6* (11), 4167−4175.
(13) Bo, R.; Taheri, M.; Liu, B.; Ricco, R.; Chen, H.; Amenitsch, H.; Fusco, Z.; Tsuzuki, T.; Yu, G.; Ameloot, R.; et al. Hierarchical Metal-Organic Framework Films with Controllable Meso/Macroporosity. *Adv. Sci.* **2020**, *7* (24), No. 2002368.
(14) Hameed, I.; Sharpe, S.; Barcklow, D.; Au-Yeung, J.; Verma, S.; Huang, J.; Barr, B.BASED-XAI: Breaking Ablation Studies Down for Explainable Artificial Intelligence. 2022, arXiv:2207.05566. arXiv.org e-Print archive. https://arxiv.org/abs/2207.05566 (accessed 10 March, 2023).
(15) Ojala, M.; Garriga, G. C. Permutation tests for studying classifier performance. *J. Mach. Learn. Res.* **2010**, *11* (6), 1833−1863.
(16) Pokhrel, S.; Birkenstock, J.; Schowalter, M.; Rosenauer, A.; Mädler, L. Growth of ultrafine single crystalline WO3 nanoparticles using flame spray pyrolysis. *Cryst. Growth Des.* **2010**, *10* (2), 632−639.
(17) Chen, H.; Bo, R.; Shrestha, A.; Xin, B.; Nasiri, N.; Zhou, J.; Di Bernardo, I.; Dodd, A.; Saunders, M.; Lipton-Duffin, J.; et al. NiO−ZnO nanoheterojunction networks for room-temperature volatile organic compounds sensing. *Adv. Opt. Mater.* **2018**, *6* (22), No. 1800677.
(18) Tricoli, A.; Nasiri, N.; Chen, H.; Wallerand, A. S.; Righettoni, M. Ultra-rapid synthesis of highly porous and robust hierarchical ZnO films for dye sensitized solar cells. *Sol. Energy* **2016**, *136*, 553−559.
(19) Bo, R.; Zhang, F.; Bu, S.; Nasiri, N.; Di Bernardo, I.; Tran-Phu, T.; Shrestha, A.; Chen, H.; Taheri, M.; Qi, S.; et al. One-step synthesis of porous transparent conductive oxides by hierarchical self-assembly of aluminum-doped ZnO nanoparticles. *ACS Appl. Mater. Interfaces* **2020**, *12* (8), 9589−9599.
(20) Samerjai, T.; Tamaekong, N.; Wetchakun, K.; Kruefu, V.; Liewhiran, C.; Siriwong, C.; Wisitsoraat, A.; Phanichphat, S. Flame-spray-made metal-loaded semiconducting metal oxides thick films for flammable gas sensing. *Sens. Actuators, B* **2012**, *171*−*172*, 43−61.
(21) Chen, H.; Bo, R.; Tran-Phu, T.; Liu, G.; Tricoli, A. One-Step Rapid and Scalable Flame Synthesis of Efficient WO3 Photoanodes for Water Splitting. *ChemPlusChem* **2018**, *83* (7), 569−576.
(22) Nasiri, N.; Ceramidas, A.; Mukherjee, S.; Panneerselvan, A.; Nisbet, D. R.; Tricoli, A. Ultra-porous nanoparticle networks: A biomimetic coating morphology for enhanced cellular response and infiltration. *Sci. Rep.* **2016**, *6* (1), No. 24305.
(23) Nordin, N. A. H. M.; Ismail, A. F.; Misdan, N.; Nazri, N. A. M. Modified ZIF-8 Mixed Matrix Membrane for CO2/CH4 Separation. *AIP Conf. Proc.* **2017**, No. 020091, DOI: 10.1063/1.5005424.
(24) Wang, S.; Jiao, Y.; Yin, J.; Liu, Y.; Li, X.; Yang, W.; Han, S.; Zhao, B.; Wu, F.; Jiang, J.; Zhang, H. Innovation synthesis of NiS quantum dots modified CdS/WO3 heterostructures as high-efficiency bifunctional photocatalysts for construction of visible light driven Z-scheme water-splitting and Cr (VI) degradation. *Appl. Surf. Sci.* **2022**, *602*, No. 154226.
(25) Soumya, K.; Selvam, I. P.; Vinod, C.; Potty, S. Tuning of work function of ZnO by doping and co-doping: An investigation using X-ray photoelectron spectroscopy. *Thin Solid Films* **2022**, *761*, No. 139538.
(26) Tian, F.; Cerro, A. M.; Mosier, A. M.; Wayment-Steele, H. K.; Shine, R. S.; Park, A.; Webster, E. R.; Johnson, L. E.; Johal, M. S.; Benz, L. Surface and stability characterization of a nanoporous ZIF-8 thin film. *J. Phys. Chem. C* **2014**, *118* (26), 14449−14456.
(27) Pi, W.; Chen, X.; Fu, Q.; Lu, Z.; Li, H.; Tang, Z.; Luo, W. The gas-sensing performance of a core−shell SnO 2-based chemiresistive MEMS sensor for H 2 S detection under vacuum. *J. Mater. Chem. C* **2023**, *11* (37), 12517−12524.
(28) Feng, C.; Li, X.; Ma, J.; Sun, Y.; Wang, C.; Sun, P.; Zheng, J.; Lu, G. Facile synthesis and gas sensing properties of In2O3−WO3 heterojunction nanofibers. *Sens. Actuators, B* **2015**, *209*, 622−629.
(29) Kim, N.-H.; Choi, S.-J.; Kim, S.-J.; Cho, H.-J.; Jang, J.-S.; Koo, W.-T.; Kim, M.; Kim, I.-D. Highly sensitive and selective acetone sensing performance of WO3 nanofibers functionalized by Rh2O3 nanoparticles. *Sens. Actuators, B* **2016**, *224*, 185−192.
(30) Righettoni, M.; Tricoli, A.; Pratsinis, S. E. Si: WO3 sensors for highly selective detection of acetone for easy diagnosis of diabetes by breath analysis. *Anal. Chem.* **2010**, *82* (9), 3581−3587.
(31) Zhou, T.; Sang, Y.; Wang, X.; Wu, C.; Zeng, D.; Xie, C. Pore size dependent gas-sensing selectivity based on ZnO@ ZIF nanorod arrays. *Sens. Actuators, B* **2018**, *258*, 1099−1106.
(32) Kim, J.-Y.; Bharath, S. P.; Mirzaei, A.; Kim, H. W.; Kim, S. S. Classification and concentration estimation of CO and NO2 mixtures under humidity using neural network-assisted pattern recognition analysis. *J. Hazard. Mater.* **2023**, *459*, No. 132153.
(33) Zhang, H.; Han, Y. A new mixed-gas-detection method based on a support vector machine optimized by a sparrow search algorithm. *Sensors* **2022**, *22* (22), No. 8977.
(34) Kroutil, J.; Laposa, A.; Ahmad, A.; Voves, J.; Povolny, V.; Klimsa, L.; Davydova, M.; Husak, M. A chemiresistive sensor array based on polyaniline nanocomposites and machine learning classification. *Beilstein J. Nanotechnol.* **2022**, *13* (1), 411−423.
(35) Shrivastava, A.; Gupta, V. B. Methods for the determination of limit of detection and limit of quantitation of the analytical methods. *Chron. Young Sci.* **2011**, *2* (1), 21−25.
(36) Liu, C.; Cohen, I.; Vishinkin, R.; Haick, H. Nanomaterial-Based Sensor Array Signal Processing and Tuberculosis Classification Using Machine Learning. *J. Low Power Electron. Appl.* **2023**, *13* (2), No. 39.
(37) Zhou, K.; Liu, Y. Early-stage gas identification using convolutional long short-term neural network with sensor array time series data. *Sensors* **2021**, *21* (14), No. 4826.
(38) Agbonlahor, O. G.; Muruganathan, M.; Banerjee, A.; Mizuta, H. Machine learning identification of atmospheric gases by mapping the

graphene-molecule van der waals complex bonding evolution. *Sens. Actuators, B* **2023**, *380*, No. 133383.
(39) Ni, W.; Wang, T.; Wu, Y.; Chen, X.; Cai, W.; Zeng, M.; Yang, J.; Hu, N.; Yang, Z. Classification and Concentration Predictions of Volatile Organic Compounds Using an Electronic Nose Based on XGBoost-Random Forest Algorithms. *IEEE Sens. J.* **2024**, *24* (1), 671−678.
(40) Acharyya, S.; Nag, S.; Guha, P. K. Ultra-selective tin oxide-based chemiresistive gas sensor employing signal transform and machine learning techniques. *Anal. Chim. Acta* **2022**, *1217*, No. 339996.
(41) Acharyya, S.; Nag, S.; Guha, P. K. Selective detection of VOCs with WO 3 nanoplates-based single chemiresistive sensor device using machine learning algorithms. *IEEE Sens. J.* **2021**, *21* (5), 5771−5778.
(42) Itoh, T.; Koyama, Y.; Shin, W.; Akamatsu, T.; Tsuruta, A.; Masuda, Y.; Uchiyama, K. Selective detection of target volatile organic compounds in contaminated air using sensor array with machine learning: Aging notes and mold smells in simulated automobile interior contaminant gases. *Sensors* **2020**, *20* (9), No. 2687.
(43) Acharyya, S.; Jana, B.; Nag, S.; Saha, G.; Guha, P. K. Single resistive sensor for selective detection of multiple VOCs employing SnO2 hollowspheres and machine learning algorithm: A proof of concept. *Sens. Actuators, B* **2020**, *321*, No. 128484.

https://doi.org/10.1021/acsami.5c02081
ACS Appl. Mater. Interfaces 2025, 17, 27408−27421